



HAL
open science

High-velocity hot CO emission close to Sgr A*

J. Goicoechea, M. Santa-Maria, D. Teyssier, J. Cernicharo, M. Gerin, J. Pety

► **To cite this version:**

J. Goicoechea, M. Santa-Maria, D. Teyssier, J. Cernicharo, M. Gerin, et al.. High-velocity hot CO emission close to Sgr A*: Herschel/HIFI*,** submillimeter spectral survey toward Sgr A*. *Astronomy and Astrophysics - A&A*, 2018, 616, pp.L1. 10.1051/0004-6361/201833684 . hal-02347744

HAL Id: hal-02347744

<https://hal.science/hal-02347744>

Submitted on 28 Apr 2023

HAL is a multi-disciplinary open access archive for the deposit and dissemination of scientific research documents, whether they are published or not. The documents may come from teaching and research institutions in France or abroad, or from public or private research centers.

L'archive ouverte pluridisciplinaire **HAL**, est destinée au dépôt et à la diffusion de documents scientifiques de niveau recherche, publiés ou non, émanant des établissements d'enseignement et de recherche français ou étrangers, des laboratoires publics ou privés.

LETTER TO THE EDITOR

High-velocity hot CO emission close to Sgr A*

Herschel/HIFI^{★,★★} submillimeter spectral survey toward Sgr A*

J. R. Goicoechea¹, M. G. Santa-Maria¹, D. Teyssier², J. Cernicharo¹, M. Gerin³, and J. Pety^{3,4}

¹ Instituto de Física Fundamental (CSIC), Calle Serrano 121, 28006 Madrid, Spain
e-mail: javier.r.goicoechea@csic.es

² Telespazio Vega UK Ltd for ESA/ESAC, Urbanización Villafranca del Castillo, Villanueva de la Cañada, 28692 Madrid, Spain

³ Sorbonne Université, Observatoire de Paris, Université PSL, École Normale Supérieure, CNRS, LERMA, 75014 Paris, France

⁴ Institut de Radioastronomie Millimétrique (IRAM), 300 rue de la Piscine, 38406 Saint Martin d'Hères, France

Received 20 June 2018 / Accepted 18 July 2018

ABSTRACT

The properties of molecular gas, the fuel that forms stars, inside the cavity of the circumnuclear disk (CND) are not well constrained. We present results of a velocity-resolved submillimeter scan ($\sim 480\text{--}1250$ GHz) and [C II] $158\ \mu\text{m}$ line observations carried out with *Herschel*/HIFI toward Sgr A*; these results are complemented by a $\sim 2' \times 2'$ ^{12}CO ($J = 3\text{--}2$) map taken with the IRAM 30 m telescope at $\sim 7''$ resolution. We report the presence of high positive-velocity emission (up to about $+300\ \text{km s}^{-1}$) detected in the wings of ^{12}CO $J = 5\text{--}4$ to $10\text{--}9$ lines. This wing component is also seen in H_2O ($1_{1,0}\text{--}1_{0,1}$), a tracer of hot molecular gas; in [C II] $158\ \mu\text{m}$, an unambiguous tracer of UV radiation; but not in [C I] 492, 806 GHz. This first measurement of the high-velocity ^{12}CO rotational ladder toward Sgr A* adds more evidence that hot molecular gas exists inside the cavity of the CND, relatively close to the supermassive black hole (< 1 pc). Observed by ALMA, this velocity range appears as a collection of ^{12}CO ($J = 3\text{--}2$) cloudlets lying in a very harsh environment that is pervaded by intense UV radiation fields, shocks, and affected by strong gravitational shears. We constrain the physical conditions of the high positive-velocity CO gas component by comparing with non-LTE excitation and radiative transfer models. We infer $T_k \simeq 400\ \text{K}\text{--}2000\ \text{K}$ for $n_H \simeq (0.2\text{--}1.0) \times 10^5\ \text{cm}^{-3}$. These results point toward the important role of stellar UV radiation, but we show that radiative heating alone cannot explain the excitation of this $\sim 10\text{--}60\ M_\odot$ component of hot molecular gas inside the central cavity. Instead, strongly irradiated shocks are promising candidates.

Key words. ISM: clouds – ISM: kinematics and dynamics – ISM: molecules – Galaxy: center

1. Introduction

The Galactic center (GC), in particular the neighborhood of the central supermassive black hole (SMBH) at Sgr A* (Schödel et al. 2002; Ghez et al. 2008; Gillessen et al. 2009), represents a unique laboratory to understand the properties of interstellar gas in extreme conditions: intense UV fields and powerful winds from massive stars, shocks, strong gravitational shears, and complicated orbital motions (Morris & Serabyn 1996; Genzel et al. 2010). The interstellar material in the innermost region of our Galaxy consists of a cavity of radius ~ 1.5 pc containing warm dust and gas, ionized by UV radiation from about 100 OB-type massive stars of the central cluster (e.g., Krabbe et al. 1995). Some of the ionized gas streamers (the mini-spiral) seem to bring material close to the very center (e.g., Zhao et al. 2009; Irons et al. 2012; Lau et al. 2013). Between ~ 1.5 pc and ~ 2.5 pc, a ring of denser molecular gas and cooler dust exists (the CND, e.g., Guesten et al. 1987; Bradford et al. 2005; Montero-Castaño et al. 2009; Requena-Torres et al. 2012; Mills et al. 2013).

* *Herschel* is an ESA space observatory with science instruments provided by European-led Principal Investigator consortia with important participation from NASA.

** Includes IRAM 30 m telescope observations. IRAM is supported by INSU/CNRS (France), MPG (Germany), and IGN (Spain).

Owing to hostile conditions inside the cavity of the CND, the presence of molecular gas was originally not expected. Recent studies, however, point toward its existence (e.g., Herrnstein & Ho 2002; Goicoechea et al. 2013; Ciurlo et al. 2016; Moser et al. 2017; Mills et al. 2017; Yusef-Zadeh et al. 2017). Indeed, obtaining high-resolution spectral images of the molecular gas emission close to Sgr A* is currently feasible with radio interferometers such as ALMA (e.g., Moser et al. 2017; Yusef-Zadeh et al. 2017). In particular, Goicoechea et al. (2018) have detected a collection of ^{12}CO ($J = 3\text{--}2$) cloudlets emitting at higher positive velocities than reported before (up to $v_{\text{LSR}} \simeq +300\ \text{km}^{-1}$). Owing to the small cloudlet sizes ($\lesssim 20\ 000$ AU), broad line profiles ($\Delta v \simeq 25\text{--}40\ \text{km s}^{-1}$), but similar line-velocity centroids over the cavity, these authors have suggested that these cloudlets are leftovers of disrupted clouds that fall into the central region. Other dissipative effects such as shocks in colliding streams, cloudlet–cloudlet collisions, colliding stellar winds, or advancing photoionization fronts, perhaps triggering gas compression and molecular gas formation, may also explain the presence of molecular gas in the cavity (Goicoechea et al. 2018).

Most of the luminosity emitted by molecular gas heated by shocks or illuminated by strong UV fields (leading to $T_k > 100$ K) is radiated in mid- J and high- J lines at submillimeter and far-IR wavelengths that are inaccessible to ground-based

telescopes. In particular, observations of the CO rotational ladder (e.g., [Indriolo et al. 2017](#); [Joblin et al. 2018](#)) are critical tools to determine the heating mechanisms and nature of the molecular gas in the GC and, in a broader context, to better understand the emission from distant active and star-forming extragalactic nuclei (e.g., [van der Werf et al. 2010](#); [Rangwala et al. 2011](#)).

2. Observations and data reduction

The spectral scan toward Sgr A* was carried out with the heterodyne receiver HIFI ([de Graauw et al. 2010](#)) on board *Herschel* ([Pilbratt et al. 2010](#)). Owing to intense molecular line emission around the CNB area, these observations were performed in the Spectral Scan Load Chop mode using an internal cold load as reference. We used the Wide Band Acousto-Optical Spectrometer, which provides a spectral resolution of 1.1 MHz and instantaneous bandwidths of 4 (2.4) GHz in bands 1–5 (6–7). The total observing time was ~ 40 h. Some of the frequency ranges were affected by isolated spurious signals, together with distorted residual baselines due to imperfect gain drift correction. While these signals were treated by the HIFI pipeline through dedicated line masking, the second artifact was corrected by fitting polynomial baselines on each spectrum prior to deconvolution ([Comito & Schilke 2002](#)). Data calibration was performed in HIPE ([Ott 2010](#)). Deconvolution allows the recovery of both line and continuum on a single side-band (SSB) intensity and frequency scale, allowing accurate absorption and emission studies. We adopted beam efficiencies and half power beam widths (HPBW) from the latest HIFI beam model¹ and used the main-beam temperature scale (T_{mb}). The rms of the SSB spectra (per 2 km s^{-1} channel) are ~ 15 , ~ 25 , ~ 40 , ~ 60 , and ~ 120 mK for bands 1–5, respectively, and ~ 175 mK for the [C II] $158 \mu\text{m}$ line. Table B.1 lists the total integrated line intensities with global uncertainties up to $\approx 15\%$, the mean velocity ($\langle v_{\text{LSR}} \rangle$), velocity dispersion ($\langle \Delta v \rangle$), and HPBW at multiple line frequencies.

We complemented pointed observation by HIFI with a $\sim 2' \times 2'$ map of the $^{12}\text{CO } J=3-2$ line (345.796 GHz) at $\sim 7''$ angular resolution, observed with the IRAM 30 m telescope (Pico Veleta, Spain) using the EMIR330 receiver and the FFTS backend at 200 kHz resolution. The map was carried by scanning, on the fly, in two orthogonal directions on the sky. Owing to very extended ^{12}CO emission in the GC, the map was taken using a nearby reference position, at $(+324'', -124'')$ with respect to Sgr A* at $(0'', 0'')$, which we successively calibrated using increasingly distant pointed observations ($\Delta\text{RA} = +1000'', +2000'', +3000'', +4000'', \text{ and } +5000''$). The total integration time was 3.6 h, leading to a rms of $\sim 1.5 \text{ K per } 2 \text{ km s}^{-1}$ channel. The spectra were baselined and gridded to a data cube through convolution with a Gaussian kernel providing a final resolution of $\sim 10''$. The total integrated intensity map is shown in Fig. 1.

3. Results: Detected lines and wing emission

We focus on the brightest detected emission lines. These include $^{12}\text{CO } (J=5-10)$ rotational lines from ^{13}CO , C^{18}O , HCO^+ , $\text{HCN } (J=6-8)$, CN , and H_2O , and fine structure lines from ionized (C^+) and neutral atomic carbon (C). Table B.1 tabulates their spectroscopic and observational parameters. Most of these were previously detected at low spectral resolution with SPIRE

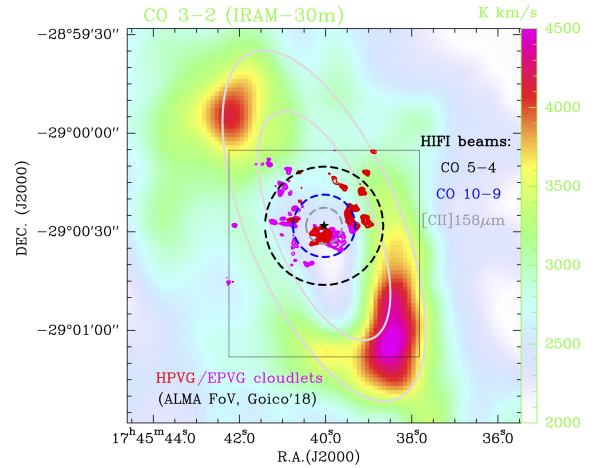


Fig. 1. $^{12}\text{CO } (J=3-2)$ integrated intensity map of the inner $2'$ of the Galaxy obtained with the IRAM 30 m telescope and dominated by emission from the CNB (color scale in K km s^{-1}). The square box shows the field of view observed by ALMA in $^{12}\text{CO } (J=3-2)$ revealing high positive-velocity cloudlets inside the cavity ([Goicoechea et al. 2018](#)). The gray curves show representative orbits CNB with 1.5 and 2.3 pc de-projected radii. The black, blue, and gray dashed circles centered at Sgr A* (black star) show HIFI's HPBWs at multiple frequencies (from $\sim 11''$ to $\sim 40''$).

and PACS ([Goicoechea et al. 2013](#)). The much higher resolution of HIFI allows us to spectrally resolve these complicated line profiles and independently study the various velocity components seen toward the GC.

In addition to emission, $\text{H}_2\text{O } 1_{1,0}-1_{0,1}$ and [C II] $158 \mu\text{m}$ lines show absorption features below the continuum level. Compared to the CNB, the continuum flux densities measured by HIFI toward Sgr A* are low, i.e., ~ 50 and $\sim 100 \text{ Jy beam}^{-1}$ at 557 and 809 GHz, respectively. This is due to the lower (and hotter) column densities of dust in the cavity ([Etxaluz et al. 2011](#)). The absorption at $v_{\text{LSR}} \approx 0 \text{ km s}^{-1}$ is produced by local diffuse clouds of the Galactic arms ([Greaves & Williams 1994](#)) and also by clouds in the GC itself (e.g., [Goto et al. 2002](#)). In addition, the $\text{H}_2\text{O } 1_{1,0}-1_{0,1}$ line shows absorption at high negative velocities, $v_{\text{LSR}} \approx -200$ to -100 km s^{-1} (seen also in [Sandqvist et al. 2003](#)), generally attributed to high negative velocity gas clouds (-180 km s^{-1} feature, [Guesten & Downes 1981](#)) and to the near side of the, historically called, expanding molecular ring (EMR or -135 km s^{-1} feature, [Scoville 1972](#)). These features are produced by diffuse, low excitation molecular gas in the inner few hundred pc of the Galaxy ([Goto et al. 2002](#)) but they are not associated with Sgr A*.

In addition to emission at $|v_{\text{LSR}}| < 150 \text{ km s}^{-1}$ (typical of the CNB), the mid- J ^{12}CO lines display a *high positive-velocity wing* (HPVW) and have emission up to $v_{\text{LSR}} \approx +270 \text{ km s}^{-1}$ (zooms in Fig. 2). The HPVW emission is faint ($\sim 500 \text{ mK}$) and is not seen in $^{13}\text{CO } (J=5-4)$, implying optically thin mid- J ^{12}CO emission. This component has not been discussed in previous observations of the CNB (e.g., [Bradford et al. 2005](#); [Requena-Torres et al. 2012](#)) but pioneering detection of broad $^{12}\text{CO } J=7-6$ line widths toward Sgr A* suggested the presence of molecular gas within the cavity ([Harris et al. 1985](#)). [Goicoechea et al. \(2013\)](#) also reported broad [O I] $63 \mu\text{m}$ emission wings toward Sgr A* (up to $\approx 300 \text{ km s}^{-1}$).

Central region ALMA images unveil the presence of small-scale $^{12}\text{CO } (J=3-2)$ cloudlets inside the cavity (shown in Fig. 1). These cloudlets emit in the same HPVW range, showing

¹ <https://www.cosmos.esa.int/web/herschel/legacy-documentation-hifi>

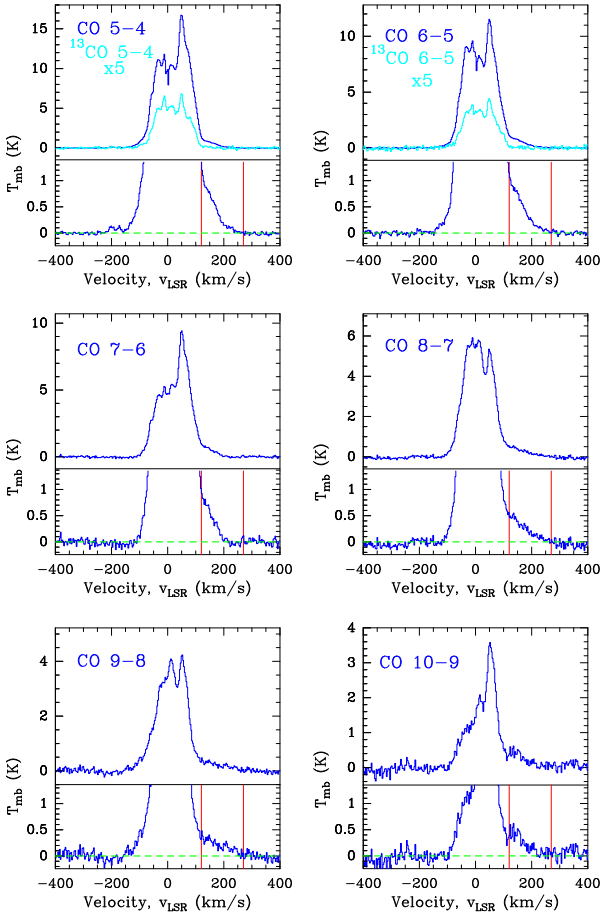


Fig. 2. Mid- J ^{12}CO and ^{13}CO lines observed with HIFI toward Sgr A* (baseline subtracted). The two red vertical lines at $v_{\text{LSR}} \approx +120$ and $+270 \text{ km}^{-1}$ delineate the HPVW emission.

independent spectral features at $v_{\text{LSR}} = +150\text{--}200 \text{ km s}^{-1}$ (high positive-velocity gas; HPVG) and at $v_{\text{LSR}} = +200\text{--}300 \text{ km s}^{-1}$ (extreme positive velocity gas; EPVG). From the CO $J = 3\text{--}2$ maps, we determine an interferometer-alone to single-dish line flux ratio of ≈ 0.2 (HPVW range). As we expect the unresolved cloudlets to be hot (Goicoechea et al. 2013; Mills et al. 2017) the contrast between emission from the extended background and these cloudlets is likely to increase for the more excited CO lines, leading to larger flux ratios. In the following we attribute the origin of the mid- J ^{12}CO HPVW emission to the same cloudlets. Their filling factor in the HIFI beams is also about 0.2.

H_2O and C^+ also show HPVW components (Fig. 3). Owing to its 11.3 eV ionization potential, the detection of $[\text{C II}] 158 \mu\text{m}$ implies that the high-velocity gas is irradiated by stellar far-ultraviolet photons (FUV; $5 \lesssim E < 13.6 \text{ eV}$). The presence of $\text{H}_2\text{O } 1_{1,0}\text{--}1_{0,1}$ HPVW emission, and of several rotationally excited H_2O lines (Goicoechea et al. 2013) suggests elevated temperatures, such as those in shocks; the gas-phase routes leading to abundant water vapor are endothermic or possess energy barriers (van Dishoeck et al. 2013). Interestingly, the atomic carbon fine-structure lines $[\text{C I}] 492, 809 \text{ GHz}$ do not show HPVW. Only the ground-state line at $\sim 492 \text{ GHz}$ displays an independent feature at $v_{\text{LSR}} \approx +165 \text{ km s}^{-1}$; the $[\text{C I}] 809 \text{ GHz}$ line is barely detected in this velocity range. This feature is traditionally associated with the back side of the EMR. Indeed, the very low $[\text{C I}] 809/492$ line intensity ratio $\lesssim 1$ of this feature (with I_{492} and

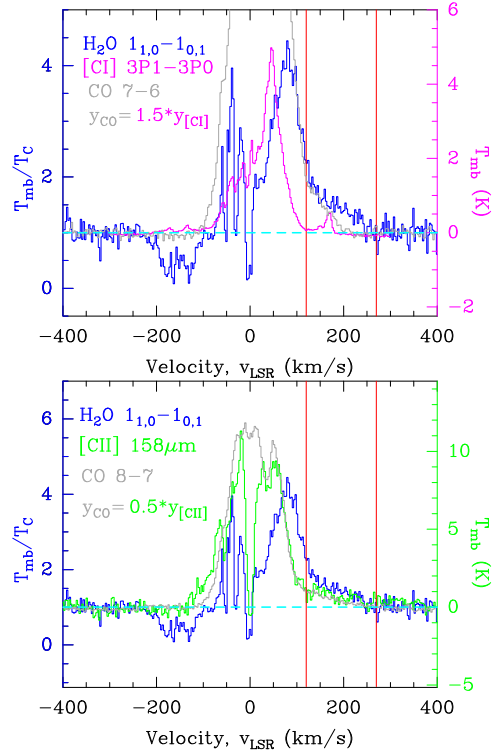


Fig. 3. HIFI multi-line detection toward Sgr A*. The two red vertical lines at $v_{\text{LSR}} \approx +120$ and $+270 \text{ km}^{-1}$ delineate the HPVW emission. The intensity scale is in T_{mb} units (baseline subtracted) except for $\text{H}_2\text{O } 1_{1,0}\text{--}1_{0,1}$ that is in $T_{\text{mb}}/T_{\text{C}}$ (divided by the continuum).

I_{809} in $\text{W m}^{-2} \text{ sr}^{-1}$) implies cold gas temperatures and thus is not related to the source of HPVW emission.

The HIFI scan also shows mid- J HCO^+ and HCN emission lines (up to $J = 8\text{--}7$). These lines do not display HPVW emission component either (Fig. B.1). Their lower velocity emission range ($|v_{\text{LSR}}| < 150 \text{ km s}^{-1}$) and high HCN/HCO^+ intensity ratios (1.6–1.7; likely enhanced by IR pumping of vibrationally excited HCN lines, see e.g., Mills et al. 2013) agree with previous maps of the CND in the same species (Montero-Castaño et al. 2009; Mills et al. 2013). Given the large size of HIFI beams at these frequencies, very likely the HCN and HCO^+ emission toward Sgr A* is beam-peaked emission from the CND.

4. Physical conditions of high-velocity CO gas

From the detection of a few low-energy rotational lines (e.g., with ALMA) it is not easy to constrain the physical conditions of the high-velocity cloudlets seen inside the cavity. With *Herschel*/HIFI we spectrally resolve the HPVW emission in several rotationally excited CO lines. From the observed lines, we determine the beam-averaged ^{12}CO column density (N) and rotational temperature (T_{rot}) associated with the HPVW component, which has line intensities integrated from $+120$ to $+270 \text{ km s}^{-1}$ (see Table B.2). Table 1 summarizes the inferred $N(^{12}\text{CO})$ and $T_{\text{rot}}(\text{mid-}J ^{12}\text{CO})$ values based on rotational diagram fits (Fig. 4). The HPVW component shows a higher degree of excitation ($T_{\text{rot}} \approx 100 \text{ K}$ versus 70 K) and more pronounced curvature than the main spectral component, i.e., total integrated line intensity minus HPVW. As for HCN and HCO^+ , signal from the mid- J ^{12}CO main component is likely dominated by emission from the CND and surroundings (Fig. 1).

Table 1. Beam-averaged rotational temperatures, column densities, and correlation coefficients obtained from rotational diagram fits.

Emission component	T_{rot} (K)	$N(^{12}\text{CO})$ (cm^{-2})	r^2
^{12}CO HPVW ^a	101(12)	$1.9(4) \times 10^{16}$ ^b	0.946
^{12}CO main component	71(4)	$6(1) \times 10^{17}$	0.986

Notes. ^(a)From $v_{\text{LSR}} = +120$ to $+270$ km s^{-1} . ^(b) $N(^{12}\text{CO}) = 9.6 \times 10^{16} \text{ cm}^{-2}$ if one assumes a uniform filling factor of 0.2.

Assuming a ^{12}CO abundance of 2×10^{-5} with respect to H nuclei (Goicoechea et al. 2018), the ^{12}CO column density inferred from the HPVW rotational diagram is equivalent to $A_V \approx 0.5$ mag of visual extinction, or 2.5 mag if we assume a uniform beam-filling factor of 0.2 for the cloudlet ensemble. These values agree with the average extinction estimated from ALMA images (Goicoechea et al. 2018) and translate to a hot molecular gas mass of ~ 10 – $60 M_{\odot}$ in the inner 1.5 pc of the Galaxy. This mass is comparable to that of neutral atomic ($\sim 300 M_{\odot}$, Jackson et al. 1993) and ionized gas ($\sim 60 M_{\odot}$, e.g., Lo & Claussen 1983) inside the central cavity.

Given the strong stellar FUV radiation field in the region ($G_0 \approx 10^{5.3}$ – $10^{4.3}$ in Habing units, Goicoechea et al. 2018), we might expect a dominant role of radiative heating. However, state-of-the-art photodissociation region (PDR) models run with the Meudon code (Le Petit et al. 2006) for $G_0 \approx 10^{4.9}$, a cosmic-ray ionization rate of $\zeta_{\text{CR}} = 10^{-15} \text{ s}^{-1}$, and constant thermal pressures $P_{\text{th}}/k = 10^8$ – 10^9 K cm^{-3} do not reproduce the shape of the HPVW CO rotational ladder, especially as J increases (see Fig. 4). Similar conclusions were anticipated by Goicoechea et al. (2013) from (velocity unresolved) observations of higher J CO lines (up to $J = 24$ – 23). These authors suggested that only a very small filling factor (< 0.05) ensemble of FUV-irradiated dense ($n_{\text{H}} \approx 10^7 \text{ cm}^{-3}$) clumps would be compatible with a dominant role of radiative heating (PDRs). However, the filling factor of the HPVW cloudlets determined from ALMA is larger and gas densities seem much lower; otherwise the cloudlets would be prominent in IR extinction maps.

In order to constrain the range of average physical conditions that reproduce the observed mid- J CO lines (HPVW component), we have run a grid of non-local, non-LTE excitation models (see Appendix A). While only for very high densities ($n_{\text{H}} > 10^7 \text{ cm}^{-3}$) the gas is close to thermalization ($T_{\text{rot}} \approx T_{\text{k}} \approx 100 \text{ K}$), at lower densities the excitation becomes subthermal ($T_{\text{rot}} = 100 \text{ K} \ll T_{\text{k}}$), the implied gas temperature is higher, and the rotational population diagram shows curvature (Neufeld 2012). Our best fit is for $T_{\text{k}} \approx 1200 \text{ K}$ and $n_{\text{H}} \approx 10^{4.5} \text{ cm}^{-3}$ (green curve in Fig. 4). This model also fits the single-dish CO $J = 3$ – 2 emission fraction expected from the spatially unresolved high-velocity cloudlets (filling factor of ≈ 0.2). We note, however, that a more accurate solution will require us to observe and spectrally resolve higher J CO lines.

Goicoechea et al. (2018) estimated (assuming $T_{\text{rot}}(\text{CO } 3-2) = 100 \text{ K}$ precisely) density peaks around $n_{\text{H}} \approx (0.2$ – $1.0) \times 10^5 \text{ cm}^{-3}$ for the cloudlets resolved by ALMA. For these densities, our non-LTE excitation models shown in Figure A.1 imply temperatures ranging from $T_{\text{k}} \approx 400$ – 2000 K . Both the elevated T_{k} and low n_{H} (compared to the local Roche density) are compatible with the non-thermal H_2 level populations inferred from IR observations with the VLT (Ciurlo et al. 2016). These T_{k} and n_{H} also agree with H_2 multi-line detections ($T_{\text{ex}}(\text{H}_2) \sim 1100 \text{ K}$,

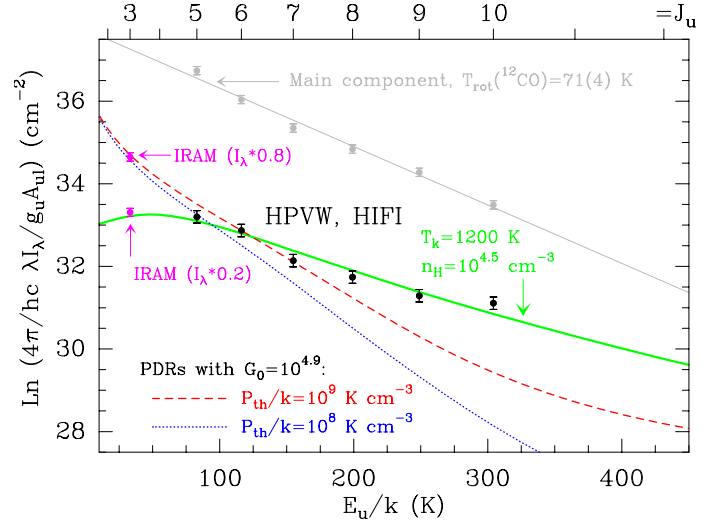


Fig. 4. Observed CO intensities of the main and HPVW components toward Sgr A* translated to rotational population diagrams. The green curve shows the best isothermal non-LTE model. The red and blue dashed curves show predictions of PDR models with $G_0 = 10^{4.9}$ and $\zeta_{\text{CR}} = 10^{-15} \text{ s}^{-1}$ (line intensities multiplied by 0.04).

Mills et al. 2017) with ISO. Infrared observations provide lower spectral resolution, thus it is difficult to extract the different velocity components independently. In summary, our observations add more quantitative evidence to the existence of high-velocity, hot molecular cloudlets inside the cavity of the CND and close to Sgr A* (< 1 pc). Although the detection of $[\text{C II}]\lambda 158 \mu\text{m}$ wing emission demonstrates the presence of FUV illumination, PDRs alone cannot drive the heating of the HPVW component. Instead, FUV-irradiated shocks, which have G_0 values that are much higher than in the models of Lesaffre et al. (2013) and Melnick & Kaufman (2015), likely dominate the heating of the hot molecular gas.

Acknowledgements. We are indebted to Tom Bell for initiating this project and for his help in the early data reduction. We thank our anonymous referee for useful comments. We also thank the Spanish MCIU and the ERC for funding support under grants AYA2017-85111-P and ERC-2013-Syg-610256-NANOCOSMOS.

References

- Balakrishnan, N., Yan, M., & Dalgarno, A. 2002, *ApJ*, 568, 443
Bradford, C. M., Stacey, G. J., Nikola, T., et al. 2005, *ApJ*, 623, 866
Carroll, T. J., & Goldsmith, P. F. 1981, *ApJ*, 245, 891
Ciurlo, A., Paumard, T., Rouan, D., & Clénet, Y. 2016, *A&A*, 594, A113
Comito, C., & Schilke, P. 2002, *A&A*, 395, 357
Cotera, A., Morris, M., Ghez, A. M., et al. 1999, *ASP Conf. Ser.*, 186, 240
de Graauw, T., Helmich, F. P., Phillips, T. G., et al. 2010, *A&A*, 518, L6
Etxaluze, M., Smith, H. A., Tolls, V., Stark, A. A., & González-Alfonso, E. 2011, *AJ*, 142, 134
Genzel, R., Eisenhauer, F., & Gillessen, S. 2010, *Rev. Mod. Phys.*, 82, 3121
Ghez, A. M., Salim, S., Weinberg, N. N., et al. 2008, *ApJ*, 689, 1044
Gillessen, S., Eisenhauer, F., Trippe, S., et al. 2009, *ApJ*, 692, 1075
Godard, B., & Cernicharo, J. 2013, *A&A*, 550, A8
Goicoechea, J. R., Pety, J., Gerin, M., et al. 2006, *A&A*, 456, 565
Goicoechea, J. R., Etxaluze, M., Cernicharo, J., et al. 2013, *ApJ*, 769, L13
Goicoechea, J. R., Pety, J., Chapillon, E., et al. 2018 *A&A*, submitted [arXiv:1806.01748]
Goto, M., McCall, B. J., Geballe, T. R., et al. 2002, *PASJ*, 54, 951
Goto, M., Geballe, T. R., Indriolo, N., et al. 2014, *ApJ*, 786, 96
Greaves, J. S., & Williams, P. G. 1994, *A&A*, 290, 259
Guesten, R., & Downes, D. 1981, *A&A*, 99, 27
Guesten, R., Genzel, R., Wright, M. C. H., et al. 1987, *ApJ*, 318, 124
Harris, A. I., Jaffe, D. T., Silber, M., & Genzel, R. 1985, *ApJ*, 294, L93

- Herrnstein, R. M., & Ho, P. T. P. 2002, [ApJ](#), 579, L83
- Indriolo, N., Bergin, E. A., Goicoechea, J. R., et al. 2017, [ApJ](#), 836, 117
- Irons, W. T., Lacy, J. H., & Richter, M. J. 2012, [ApJ](#), 755, 90
- Jackson, J. M., Geis, N., Genzel, R., et al. 1993, [ApJ](#), 402, 173
- Joblin, C., Bron, E., Pinto, C., et al. 2018, [A&A](#), 615, A129
- Krabbe, A., Genzel, R., Eckart, A., et al. 1995, [ApJ](#), 447, L95
- Lau, R. M., Herter, T. L., Morris, M. R., Becklin, E. E., & Adams, J. D. 2013, [ApJ](#), 775, 37
- Le Petit, F., Nehmé, C., Le Bourlot, J., & Roueff, E. 2006, [ApJS](#), 164, 506
- Lesaffre, P., Pineau des Forêts, G., Godard, B., et al. 2013, [A&A](#), 550, A106
- Lo, K. Y., & Claussen, M. J. 1983, [Nature](#), 306, 647
- Melnick, G. J., & Kaufman, M. J. 2015, [ApJ](#), 806, 227
- Mills, E. A. C., Güsten, R., Requena-Torres, M. A., & Morris, M. R. 2013, [ApJ](#), 779, 47
- Mills, E. A. C., Togi, A., & Kaufman, M. 2017, [ApJ](#), 850, 192
- Montero-Castaño, M., Herrnstein, R. M., & Ho, P. T. P. 2009, [ApJ](#), 695, 1477
- Morris, M., & Serabyn, E. 1996, [ARA&A](#), 34, 645
- Moser, L., Sánchez-Monge, Á., Eckart, A., et al. 2017, [A&A](#), 603, A68
- Neufeld, D. A. 2012, [ApJ](#), 749, 125
- Ott, S. 2010, [ASP Conf. Ser.](#), 434, 139
- Pilbratt, G. L., Riedinger, J. R., Passvogel, T., et al. 2010, [A&A](#), 518, L1
- Rangwala, N., Maloney, P. R., Glenn, J., et al. 2011, [ApJ](#), 743, 94
- Requena-Torres, M. A., Güsten, R., Weiß, A., et al. 2012, [A&A](#), 542, L21
- Sandqvist, A., Bergman, P., Black, J. H., et al. 2003, [A&A](#), 402, L63
- Schödel, R., Ott, T., Genzel, R., et al. 2002, [Nature](#), 419, 694
- Scoville, N. Z. 1972, [ApJ](#), 175, L127
- van der Werf, P. P., Isaak, K. G., Meijerink, R., et al. 2010, [A&A](#), 518, L42
- van Dishoeck, E. F., Herbst, E., & Neufeld, D. A. 2013, [Chem. Rev.](#), 113, 9043
- Yang, B., Stancil, P. C., Balakrishnan, N., & Forrey, R. C. 2010, [ApJ](#), 718, 1062
- Yusef-Zadeh, F., Wardle, M., Kunneriath, D., et al. 2017, [ApJ](#), 850, L30
- Zhao, J.-H., Morris, M. R., Goss, W. M., & An, T. 2009, [ApJ](#), 699, 186

Appendix A: Non-local, non-LTE excitation isothermal models

To constrain the range of plausible physical conditions that reproduce the mid- J CO line excitation and inferred $T_{\text{rot,HPVW}}$ values, we run a grid of non-local and non-LTE models (Monte Carlo model in Appendix of Goicoechea et al. 2006). We included $^{12}\text{CO-H}_2$ and $^{12}\text{CO-H}$ rotationally inelastic collisions (Yang et al. 2010; Balakrishnan et al. 2002) and assumed a molecular gas fraction of 90%, $n(\text{H}) = 0.25 n(\text{H}_2)$; this value is consistent with a strongly FUV-irradiated gas in which not all hydrogen is in molecular form. We adopted a non-thermal velocity dispersion of $\Delta v = 35 \text{ km s}^{-1}$ (from turbulence and macroscopic gas motions). This value is the observed average linewidth of the cloudlets detected by ALMA. We take the same $N(^{12}\text{CO})$ obtained from the rotational diagram and search for the range of T_{k} and $n_{\text{H}} = n(\text{H}) + 2n(\text{H}_2)$ values that reproduce the derived $T_{\text{rot,HPVW}} \approx 100 \text{ K}$ and observed line intensities.

Figure A.1 shows isothermal model results in the form of iso- T_{rot}^* contours. For each model we created rotational diagrams and determined a rotational temperature (T_{rot}^*) by fitting a straight line² to the synthetic CO line intensities in the $J_{\text{up}} = 5-10$ range. To estimate the fit goodness we calculated the minimum rms value of $\log_{10}(I_{\text{HIFI}}/I_{\text{mod}})$. Figure A.1 shows rms_{min}/rms contours of 1, 0.95 and 0.9 in magenta, red, and blue, respectively. The best model (rms = 0.076, indicated with a star in the figure) implies $T_{\text{k}} \approx 1200 \text{ K}$ and $n_{\text{H}} \approx 10^{4.5} \text{ cm}^{-3}$, but we note that a more accurate solution would require velocity-resolved observations of higher J CO lines.

Given the intense IR, visible, and UV radiation fields in the cavity, one may consider whether radiative pumping to CO vibrational and electronic levels can influence the emergent rotationally excited line intensities. For moderate gas densities ($>10^4 \text{ cm}^{-3}$) inelastic collisions are important drivers of CO rotational excitation. Thus very strong mid-IR fields are needed to alter the rotational level populations (e.g., Carroll & Goldsmith 1981; Godard & Cernicharo 2013). The estimated mid-IR color temperatures in the cavity range from $\approx 200 \text{ K}$ (Cotera et al. 1999) to 145–85 K (Lau et al. 2013). These values are around the 160 K threshold estimated by Carroll & Goldsmith (1981) for CO pumping in the no-collision limit. Hence, we suspect that IR pumping can contribute locally, around evolved stars or in protostellar envelopes, but does not drive the excitation of the optically thin mid- J CO lines we detect at high velocities. Indeed, IR observations toward the cavity do not report high positive-velocity features in the wings of the saturated $^{12}\text{CO } \nu = 1-0$ rovibrational lines (Goto et al. 2014).

Similarly, visible/UV pumping may have some relevance in strongly irradiated environments. Visible/UV pumping (included in the PDR models shown in Fig. 4) can enhance the intensity of the CO rotationally excited lines only by a factor of a few (Godard & Cernicharo 2013). Either way, these radiative excitation processes further decrease the density of the HPVW gas component below our estimation from the grid of non-LTE excitation models. Therefore, the high gas density solutions, $n_{\text{H}} \approx 10^7 \text{ cm}^{-3}$ (shown in Fig. A.1), do not seem favored for the molecular gas in the cavity.

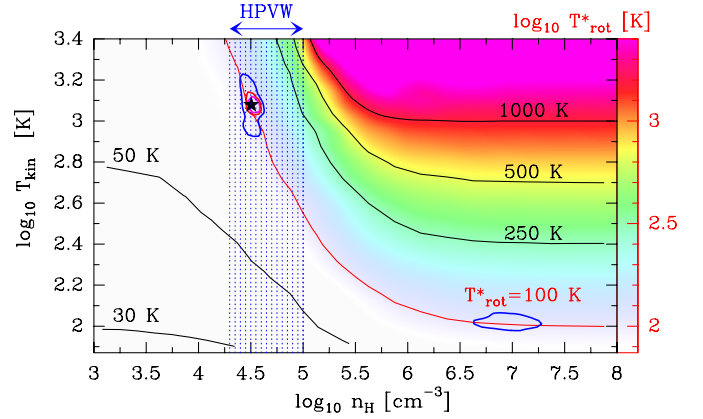


Fig. A.1. ^{12}CO rotational temperatures (T_{rot}^* , computed by fitting a straight line to synthetic line intensities in the $J_{\text{up}} = 5-10$ range) obtained from isothermal non-LTE models. The red curve shows the parameter space that reproduces the observed T_{rot} of the HPVW component. The blue-shaded area shows the estimated gas density of the high-velocity cloudlets detected by ALMA (Goicoechea et al. 2018). The magenta, red, and blue curves show rms_{min}/rms contours of 1, 0.95, and 0.9 respectively, where rms refers to the value of $\log_{10}(I_{\text{HIFI}}/I_{\text{mod}})$.

Appendix B: Complementary figures and tables

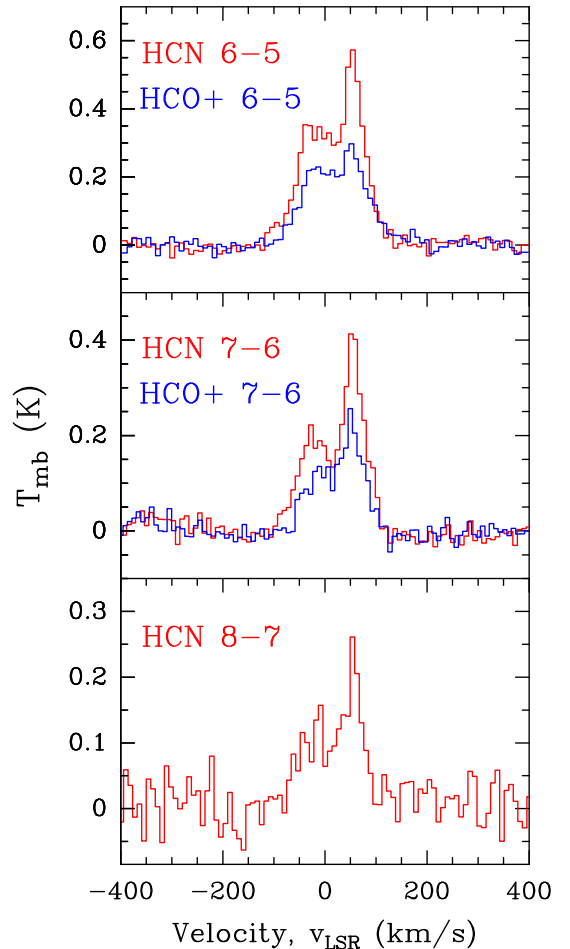


Fig. B.1. HIFI detection of HCN and HCO⁺ lines toward Sgr A* showing emission only at velocities typical of the CND ($v_{\text{LSR}} < 150 \text{ km s}^{-1}$).

² At low densities, $n_{\text{H}} \ll n_{\text{cr}}(J)$, CO rotational level populations are such that plotted in a rotational diagram they show considerable curvature (Neufeld 2012). We also fit these models with a straight line.

Table B.1. Spectroscopic and observational parameters of the lines discussed in this work.

Species	Transition	Frequency (GHz)	E_u/k (K)	A_{ul} (s^{-1})	Intensity ^a , I ($W m^{-2} sr^{-1}$)	$\langle v \rangle^b$ ($km s^{-1}$)	$\langle \Delta v \rangle^c$ ($km s^{-1}$)	Beam (arcsec)	Herschel ObsID
C ⁺	$^2P_{3/2-2}P_{1/2}$	1900.53690	91.2	2.3×10^{-6}	8.56×10^{-6}	22.0	155.3	11	1342243685
C	$^3P_{2-3}P_1$	809.90231	62.5	2.7×10^{-7}	1.83×10^{-7}	18.4	135.1	26	1342230279
	$^3P_{1-3}P_0$	492.50139	23.6	7.9×10^{-8}	4.73×10^{-8}	24.0	155.3	42	1342249609
CO	$J = 10-9$	1151.98544	304.2	1.0×10^{-4}	5.00×10^{-7}	32.0	132.2	19	1342251185
	$J = 9-8$	1036.91239	248.9	7.5×10^{-5}	6.27×10^{-7}	17.1	123.2	20	1342243700
	$J = 8-7$	921.79970	199.1	5.2×10^{-5}	6.05×10^{-7}	18.3	148.6	23	1342243707
	$J = 7-6$	806.65180	154.9	3.5×10^{-5}	5.14×10^{-7}	31.3	118.2	26	1342230279
	$J = 6-5$	691.47208	116.2	2.2×10^{-5}	4.79×10^{-7}	21.6	131.7	30	1342239594
	$J = 5-4$	576.26793	83.0	1.2×10^{-5}	3.83×10^{-7}	23.4	129.1	36	1342230394
	$J = 6-5$	661.06728	111.1	1.9×10^{-5}	3.08×10^{-8}	13.6	143.0	32	1342239594
^{13}CO	$J = 5-4$	550.92628	79.3	1.1×10^{-5}	3.28×10^{-8}	14.6	161.4	38	1342249609
$C^{18}O$	$J = 5-4$	548.83101	79.0	1.1×10^{-5}	2.41×10^{-9}	71.9	92.8	38	1342249609
CN	$N, J = 5, 11/2-4, 9/2$	566.94721	81.6	1.9×10^{-3}	5.50×10^{-9}	44.7	130.3	37	1342249609
HCN	$J = 8-7$	708.87700	153.1	1.7×10^{-2}	8.74×10^{-9}	37.6	110.4	30	1342239594
HCN	$J = 7-6$	620.30400	119.1	1.2×10^{-2}	4.45×10^{-9}	31.3	90.6	34	1342230394
HCN	$J = 6-5$	531.71635	89.3	7.2×10^{-3}	5.82×10^{-9}	28.8	92.4	39	1342249609
HCO ⁺	$J = 7-6$	624.20836	119.8	2.0×10^{-2}	4.45×10^{-9}	30.2	112.0	33	1342230394
HCO ⁺	$J = 6-5$	535.06158	89.9	1.2×10^{-2}	5.82×10^{-9}	30.8	119.4	39	1342249609
$o\text{-H}_2O$	$J_{Kk} = 1_{10}-1_{01}$	556.93600	26.7	3.5×10^{-3}	9.28×10^{-9}	68.8	149.0	37	1342249609

Notes. ^(a)Moment 0 or total line intensity over each emission profile $I = \sum I(v)\Delta v$. Total uncertainty up to $\sim 10\%$. ^(b)Moment 1: Intensity-weighted mean velocity $\langle v \rangle = \sum I(v)v / \sum I(v)$. ^(c)Moment 2: Intensity-weighted velocity dispersion $\langle \Delta v \rangle = \sqrt{\frac{\sum [I(v)(v-M1)^2]}{\sum I(v)}}$.

Table B.2. Line intensities for the HPVW component.

Species	Transition	Intensity ^a , I ($W m^{-2} sr^{-1}$)
CO	$J = 10-9$	4.26×10^{-8}
	$J = 9-8$	3.00×10^{-8}
	$J = 8-7$	2.62×10^{-8}
	$J = 7-6$	2.00×10^{-8}
	$J = 6-5$	1.92×10^{-8}
	$J = 5-4$	1.08×10^{-8}
C ⁺	$^2P_{3/2-2}P_{1/2}$	1.49×10^{-8}
$o\text{-H}_2O$	$J_{Kk} = 1_{10}-1_{01}$	1.86×10^{-9}

Notes. ^(a)Integrated from $v_{LSR} = +120-270 km s^{-1}$. Total uncertainty up to $\sim 15\%$.